

Effect of geometrical parameters of reentry capsule over flowfield at high speed flow

R. C. Mehta*

Department of Aeronautical Engineering, Noorul Islam University, Kumaracoil, 629180, India

(Received August 29, 2016, Revised February 13, 2017, Accepted February 28, 2017)

Abstract. The main purpose of the paper is to analyze effect of geometrical parameters of the reentry capsules such as radius of the spherical cap, shoulder radius, back shell inclination angle and overall length on the flow field characteristics. The numerical simulation with viscous flow past ARD (Atmospheric Reentry Demonstrator), Soyuz (Russian) and OREX (Orbital Reentry EXperimental) reentry capsules for freestream Mach numbers range of 2.0-5.0 is carried out by solving time-dependent, axisymmetric, compressible laminar Navier-Stokes equations. These reentry capsules appear as bell, head light and saucer in shape. The flow field features around the reentry capsules such as bow shock wave, sonic line, expansion fan and recirculating flow region are well captured by the present numerical simulations. A low pressure is observed immediately downstream of the base region of the capsule which can be attributed to fill-up in the growing space between the shock wave and the reentry module. The back shell angle and the radius of the shoulder over the capsule are having a significant effect on the wall pressure distribution. The effects of geometrical parameters of the reentry capsules will be a useful input for the calculation of ballistic coefficient of the reentry module.

Keywords: aerodynamic; CFD; reentry capsule; shock wave; space vehicle; supersonic speed

1. Introduction

The primary design consideration of the reentry capsules requires large spherical nose radius and forebody diameter yields high aerodynamic drag. A high-speed flow-past a reentry capsule generates a bow shock wave which causes a high surface pressure and as a result the development of high aerodynamic drag which is required for aero-braking purposes. The bow shock wave is detached from the blunt fore-body and is having a mixed subsonic-supersonic region. The wall pressure distribution, the location of the sonic line and shock stand-off distance on the spherical cap region have been analytically calculated at very high speeds with an adiabatic index near to unity which gives a singular point at 60° from the stagnation point (Chester 1956, Freeman 1956). The analytical approach for the high-speed flow over the blunt-body is considerably difficult and complex (Lighthill 1957). The flow-field over the reentry capsule becomes further complicated due to the presence of corner at the shoulder and shape of the base shell of the reentry module.

An aerodynamic analysis of the commercial experiment transport (COMET) reentry capsule

*Corresponding author, Professor, E-mail: drrakhab.mehta@gmail.com

has been carried out by Wood *et al.* (1996) solving the laminar thin layer Navier-Stokes LAURA code for low supersonic to hypersonic speeds. Yamamoto and Yoshioka (1995) carried out flow field computation over the OREX (orbital reentry experiments) using computational fluid dynamics approach coupled with the thermal response of the heat shield material using finite element method in conjunction with the aerodynamic flight data. The aerodynamic characterization of the CARINA reentry module in the low supersonic Mach regimes has been performed employing numerical and experimental methods (Solazzo *et al.* 1994). The flow field simulations over the Beagle-2 spacecraft have been carried out by Liever *et al.* (2003) using CFD-FASTRAN code for low supersonic to hypersonic speeds. Mehta (2008) has carried out numerical computations over various space vehicle capsules in conjunction with satellite launch vehicle and reentry capsule.

Wind tunnel testing of the Orion crew module has been carried out by Ross *et al.* (2011) to obtain the aerodynamic and aeroacoustic. Murphy *et al.* (2011) have presented experimental static aerodynamic data for the Orion Crew Module capsule and analyzed with surface visualization and computational results. Shape optimization design method has been presented by Zhenmiz (2011) for the conceptual design of reentry capsules. Ali *et al.* (2012) have studied effects of nose-bluntness ratio on the aerodynamic performance of reentry capsules. CFD analyses of space vehicle are performed employing H3NS and FLUENT code by Viviani *et al.* (2015) to analyze the flow field over various capsules. Chen *et al.* (2015) have carried out numerical simulation of flow field for aerodynamic design of reentry capsule. Weiland (2014) has presented aerodynamic characteristics of non-winged capsules such as Apollo, Soyuz, ARD, Huygens, Beagle 2, OREX, VIKING, CARINA, and AFE.

The sphere space capsule gives the highest possible volumetric efficiency but does not able to give good manoeuvre ability. Therefore reentry space vehicle requires a back shell with inclination in order to generate lift to reduce accelerating forces on the crew tolerance levels. Bedding *et al.* (1992) have illustrated sixteen space vehicles in which the frontal diameter D of the capsule is kept constant for all configurations and varying geometrical parameters α_N , R_C , α_B , and L in three groups. In the first group, five capsules having variation in the back shell angle α_B in the range of 0° to 30° . In the second group, five capsules are having variation of the overall length varied from $1.0 D$ – $0.375 D$. In the last group the back shell angle α_B , overall length L , and shoulder radius R_C , alignment with frontal cap are varied to evaluate the ballistic performance. Recently Minenkol *et al.* (2015) have studied effect of geometrical parameter on aerodynamic performance of the space vehicles such as the Apollo and the Soyuz.

The nominal Orion crew module geometry is based on the Apollo configuration, consisting of a spherical heat shield transitioning to a conical back shell with a truncated base to accommodate docking hardware. The aerodynamic characteristic of the Orion is analyzed numerically by Stremel *et al.* (2011). The Orion is having similar in shape to the Apollo Command Module but is approximately 29% larger by length. The ARD resembles a 70% scaled version of Apollo capsule (Walpot 2001). Flow field over reentry capsules at high speed has been obtained employing Fluent software by Prasad *et al.* (2012). Pezzella *et al.* (2015) have carried out aerodynamic analysis of high speed reentry capsules.

It is worth to mention here that considerable difficulties are experienced to obtain aerodynamic data from wind-tunnel testing due to sting interference effects. The shock tunnel is having short duration of testing time. The free flight experiments, a scaled model shot inside a range and orthogonal shadowgraphs are taken as the capsule fly by each shadow graph station. The CFD approach will provide flow field behaviour and aerodynamic coefficients.

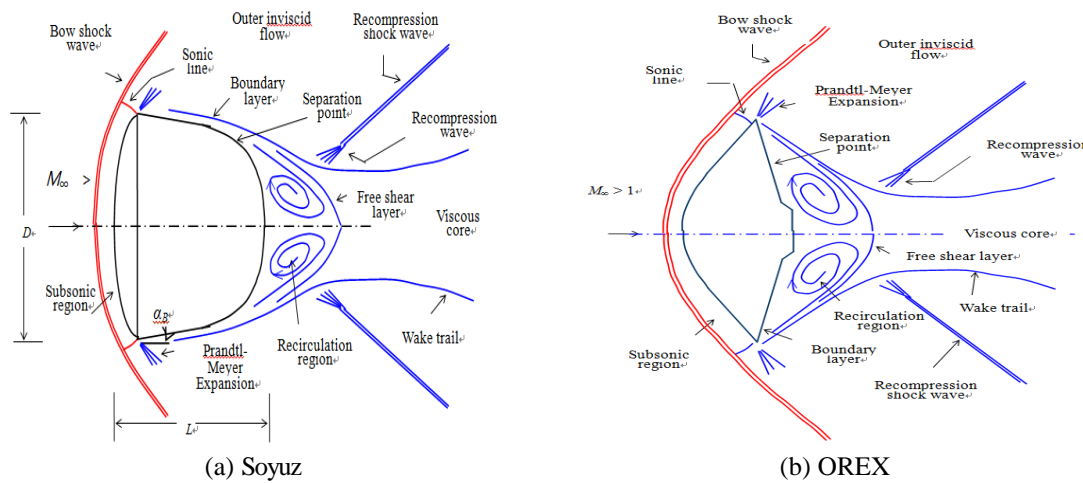


Fig. 1 Representation of flow features on Soyuz reentry module at supersonic speeds

The above literature survey reveals that the reentry capsules can be classified as a head-light as in the case of Soyuz, or bell shape as in the case of Apollo and ARD, or a saucer type as in the case of OREX. The flow field features over the reentry capsule can be delineated through the experimental and theoretical investigations at high speed. The significant flowfield features are described in Fig. 1(a) and (b) for the Soyuz and the OREX capsules, respectively. Fig. 1 leads to the necessity to investigate the influence of the geometrical parameters such as D , α_N , R_C , α_B , and L on the flow field and aerodynamic characteristics. The significant flowfield characteristics are described by the following. In the forebody region, the fluid decelerates through the bow shock wave depending on the cruise speed and altitude. As the shoulder of the capsule, the flow turns and expands rapidly and boundary layer detached, forming a free shear layer that separates the inner recirculating flow region behind the base from the outer flow field. The latter is recompressed and turned back to the freestream direction, first by the so-called lip shock, and further downstream by recompression shock. At the end of the re-circulating flow past the neck, the shear layer develops in the wake trail. A complex inviscid wave structure often includes a lip shock wave (associates with the corner expansion) and wake trail (adjacent to the shear layer confluence). The corner expansion process is a Prandtl-Meyer pattern changed by the presence of the approaching boundary layer and radius of the shoulder, R_C . The wake flow features show several known flow features such as shear layers, neck region and recompression shocks.

In the present work, numerical studies were undertaken for a freestream supersonic Mach numbers of 2.0-5.0. The numerical simulation to solve the axisymmetric laminar compressible unsteady Navier-Stokes equations is by solved on a mono-block structured grid. Surface pressure variations over the capsules are computed numerically, which will give a systematic understanding of the flow features at supersonic Mach numbers. It will also reveal the effect of geometrical parameters on aerodynamic drag. The effects of the module geometrical parameters, such as radius of the spherical cap radius, shoulder radius, cone angle and back shell inclination angle on the flow field, which will provide a useful input to obtain the ballistic coefficient of the reentry module.

2. Problem definition and approach

2.1 Governing equations

The fluid dynamics equations describing a flowfield around a space vehicle deals with balance equations for mass, momentum, and total energy. A numerical solution of the time-dependent, compressible, axisymmetric Reynolds-averaged Navier-Stokes (RANS) equation is employed to analyze the flow past the reentry modules. To capture shocks and discontinuities, the RANS equations are written in conservation form as

$$\frac{\partial \mathbf{U}}{\partial t} + \frac{\partial \mathbf{F}}{\partial x} + \frac{1}{r} \frac{\partial (r\mathbf{G})}{\partial r} + \frac{\mathbf{H}}{r} = 0 \quad (1)$$

where

$$\mathbf{U} = \begin{bmatrix} \rho \\ \rho u \\ \rho v \\ \rho E \end{bmatrix}, \quad \mathbf{F} = \begin{bmatrix} \rho u \\ \rho u^2 + p - \sigma_{xx} \\ \rho uv - \tau_{rx} \\ (\rho E + p)u - u\sigma_{xx} - v\tau_{rx} + q_x \end{bmatrix}, \quad \mathbf{G} = \begin{bmatrix} \rho v \\ \rho uv - \tau_{xr} \\ \rho v^2 + p - \sigma_{rr} \\ (\rho E + p)v - u\sigma_{xr} - v\sigma_{rr} + q_r \end{bmatrix}, \quad \mathbf{H} = \begin{bmatrix} 0 \\ 0 \\ \sigma_+ \\ 0 \end{bmatrix}$$

The viscous terms in the above equations become

$$\sigma_{xx} = -\mu \left(\frac{2}{3} \nabla \cdot \phi + 2 \frac{\partial u}{\partial x} \right)$$

$$\sigma_{rr} = -\mu \left(\frac{2}{3} \nabla \cdot \phi + 2 \frac{\partial v}{\partial r} \right)$$

$$\tau_{rx} = \tau_{xr} = \mu \left(\frac{\partial u}{\partial r} + \frac{\partial v}{\partial x} \right)$$

$$\sigma_+ = -p - \frac{2}{3} \mu \nabla \cdot \phi + 2\mu \frac{v}{r}$$

$$\nabla \cdot \phi = \frac{\partial u}{\partial x} + \frac{\partial v}{\partial r} + \frac{v}{r}$$

$$q_x = -k \frac{\partial T}{\partial x}$$

$$q_r = -k \frac{\partial T}{\partial r}$$

where σ_{xx} , σ_{rr} , σ_{xr} and σ_+ are components of the shear stress, q_x and q_r the components of heat flux vector. ϕ is the mean stream velocity. T is related to p and ρ by the perfect gas equation of state as

$$p = (\gamma - 1) \rho \left[E - \frac{1}{2} (u^2 + v^2) \right] \quad (2)$$

The ratio of the specific heats is assumed constant and is equal to 1.4. The coefficient of molecular viscosity is calculated according to Sutherland's law. The flow is assumed to be laminar, which is consistent with numerical simulation of (Liever *et al.* 2003, Mehta 2006a and Viviani *et al.* 2015).

2.2 Numerical scheme

To facilitate the spatial discretization in numerical technique, the governing fluid dynamics Eq.

Table 1 Trajectory points and initial conditions

M_∞	p_∞ , Pa	T_∞ , K
2.0	2891	219
3.0	2073	224
5.0	1238	232

(1) can be written in the integral form over a finite computational domain as

$$\frac{d}{dt} \int_{\Omega} U d\Omega + \int_{\Gamma} (\mathbf{F}dx - \mathbf{G}dr) + \int_{\Omega} \mathbf{H}d\Omega = 0 \quad (3)$$

where Ω is the computational domain, Γ is the boundary of the domain. The contour integration around the boundary of the cell is taken in anticlockwise sense. The code employs a finite volume discretization technique. Spatial and temporal terms are decoupled using the method of lines. The spatial computational domain is divided into a number of quadrilateral cells on a structured single block grid. The conservation variables within the computational cell are represented by their average value at the cell centre (i, j) . The conservative variables \mathbf{U} within each cell are calculated from their average values at the cell centre. The flux vectors \mathbf{F} and \mathbf{G} , and source vector \mathbf{H} of Eq. (1) are computed on each side of the cell (Peyret *et al.* 1983). A system of ordinary differential equations in time is obtained after integrating Eq. (1) over a computational cell and summing the flux vector on each side of the cell. The finite volume code constructed in this manner reduces to a central-difference scheme and is second-order accurate in space provided that the grid is smooth enough. Temporal integration is carried out using three-stage Runge-Kutta time-stepping method (Jameson *et al.* 1981). Artificial dissipation is added to Eq. (2) to eliminate undamped modes and to capture shocks without pre-shock oscillations. Following Jameson *et al.* (1981) a combination of second and fourth differences is employed, with the second difference being controlled by a pressure sensor. The viscous fluxes are calculated by central differencing, i.e., computing the gradients of flow variables at cell interfaces by means of Gauss theorem. The method is second-order accurate in space.

Local time-steps are used to accelerate convergence to a steady state solution by advancing the time-step at each grid point with the maximum permissible time-step allowed by the local Courant-Friedrichs-Lewy (CFL) condition. The numerical scheme is stable for a Courant number less than or equal to 2. The numerical algorithm is second-order accurate in space and time discretization. A global time-step was used and is computing using following expression

$$\Delta t = \min \left[\frac{|u|}{\Delta x} + \frac{|v|}{\Delta r} + c \sqrt{\frac{1}{(\Delta x)^2} + \frac{1}{(\Delta r)^2}} \right]^{-1} \quad (4)$$

2.3 Initial and boundary conditions

The freestream conditions for each trajectory point are enumerated in Table 1 which is used as the initial conditions. M , p and T represent Mach number, pressure and temperature, respectively.

The free flow value is used to initialize the whole flow field.

Four types of boundary conditions are required for the computation of flow field, i.e., wall, inflow, outflow and symmetric conditions. At the wall, no-slip condition is enforced by setting

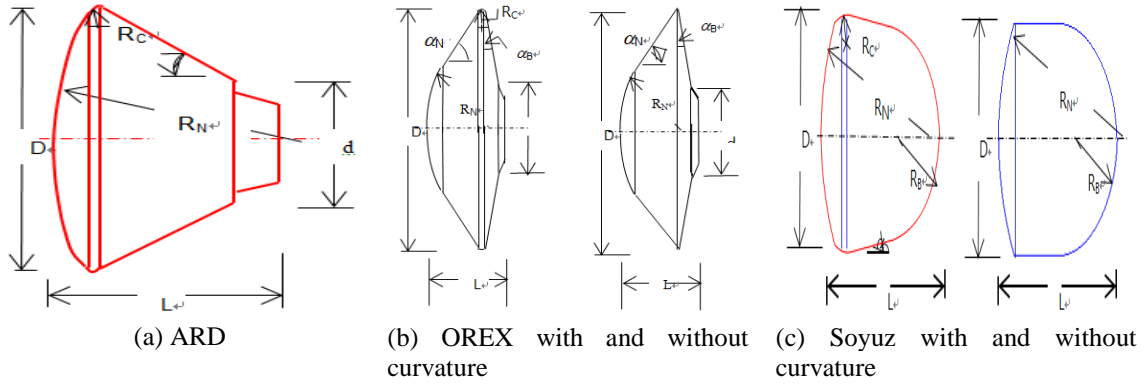


Fig. 2 Dimensional details of the reentry modules

Table 2 Geometrical parameters of reentry capsule

Capsule	Spherical radius R_N	Frontal diameter D	Corner radius R_C	Overall length L	Semi-cone angle α_N deg	Back-shell angle α_B deg
ARD	3.36	2.8	0.014	2.04	–	33.0
OREX smooth shoulder	1.35	3.40	0.001	1.508	50.0	15.0
OREX sharp shoulder	1.35	3.457	–	1.508	50.0	15.0
Soyuz smooth shoulder	2.235	2.142	0.014	2.142	–	7.0
Soyuz sharp shoulder	2.235	2.2	–	2.142	–	–

$$u_w = v_w = 0 \quad (5)$$

together with an adiabatic wall condition where subscript w refer to the wall condition. At the inflow, all the flow variables are prescribed at the freestream values as tabulated in Table 1.

At the centre line of the computational domain, the following symmetric conditions are prescribed

$$\begin{aligned} \rho v &= 0 \\ \frac{\partial u}{\partial r} &= \frac{\partial p}{\partial r} = \frac{\partial T}{\partial r} = 0 \end{aligned} \quad (6)$$

For the supersonic outflow case, all flow variables are extrapolated at the outer and wake regions of the computational domain from the vector of conserved variables \mathbf{U} as

$$\begin{aligned} \mathbf{U}_{nx,j} &= 2\mathbf{U}_{nx-1,j} - \mathbf{U}_{nx-2,j} \\ \mathbf{U}_{i,nr} &= 2\mathbf{U}_{i,nr-1} - \mathbf{U}_{i,nr-2} \end{aligned} \quad (7)$$

where the subscripts nx and nr represent the last grid points on the boundaries.

3. Geometrical detail of the reentry modules

Table 2 and Fig. 2 depict the dimensions of the space vehicles considered in the numerical

simulation. The dimensional detail of the ARD capsule, shown in Fig. 2(a), is an axisymmetric design with a spherical blunt body nose diameter, $D=2.8$ m, spherical cal radius, $R_N=3.36$ m and a shoulder radius, $R_C=0.014$ m. The back shell has inclination angle, $\alpha_B=33^\circ$ relative to the vehicle's axis of symmetry. A frustum of cone of radius 0.507 m with a 12° half angle cone is attached to the base region. The over-all length of the module $L=2.04$ m. The Dimension of the ARD is same as those investigated by Liever *et al.* (2003).

The OREX geometry is shown with and without shoulder radius in Fig. 2(b). The fore body shape consists of $R_N=1.35$ m, $\alpha_N=50^\circ$, $D=3.4$ m. $L=1.508$ m and $R_C=0.01$. The OREX geometry incorporates a rear cover with a small backward facing step at the junction between back cover and heat shield. The aft body is having a $\alpha_B=15^\circ$, half-angle relative to the plane of symmetry. The dimension of the OREX is adapted from (Yamamoto *et al.* 1995).

The dimensional detail of the Soyuz capsule (Ivanov 1994, Minenko *et al.* 2015) is having an axisymmetric shape with a spherical blunt nose diameter, $D=2.2$ m, spherical cap radius, $R_N=2.235$ m. Fig. 2(c) shows the capsule geometry with and without shoulder radius, respectively. The other capsule is also having $D=2.142$ m but with a rounded shoulder of radius, $R_C=0.014$ m. The back shell has inclination angle $\alpha_B=7^\circ$ relative to the capsule's axis of symmetry. A frustum of cone of radius is 3.624 m. The overall length of both the capsule is $L=2.142$ m. Fig. 2(c) is having $\alpha_B=0$ and with sharp shoulder.

4. Computational grid

One of the controlling factors for the numerical simulation is the proper grid arrangement. The grid points are generated by a homotopy scheme (Shang 1981) in conjunction with finite element method (Mehta 1998). Grid-independence tests are carried out, taking into consideration the effect of the computational domain, the stretching factor to control the grid intensity near the wall, and the number of grid points in the axial and normal directions. The typical computational space over the re-entry capsule is defined by a number of grid points in cylindrical coordinate system. Using these surface points as the reference nodes, the normal coordinate is then described by exponentially stretched field points extending outwards up to an outer computational boundary. These stretched grids are generated in an orderly manner. The outer boundary of the computational domain is varied from 5 to 12 times the maximum diameter of the capsule. The grid stretching factor is varied from 1.5 to 5. The grid stretching factor is selected as 5, and the outer boundary of the computational domain is kept about 4-7 times the maximum diameter of the reentry capsule. In the downstream direction, the computational boundary is about 6-10 times the maximum diameter of the capsule.

The grid used consists of 80 cells in the body-normal direction and 40 cells circumferentially. A close-up view of axisymmetric mesh can be seen in Fig. 3. The finer mesh in the vicinity of wall helps to resolve the viscous effects. The grid size varies depending on freestream Mach number. The minimum mesh size in the normal direction of the capsule is kept about 1.488×10^{-4} m.

The number of grid points in the shoulder region is large enough to capture the rapid expansion that the flow experienced locally and, then, to accurately predict the rapid expansion that the flow separation and the angle of the resulting shear layer. There are also sufficient points in the separated flow region to resolve the vertical structure at the beginning of the wake flow. The computation grid is found to give a relative difference of about $\pm 3\%$ in the computation of aerodynamic drag coefficient. The convergence criterion is based on the difference in density

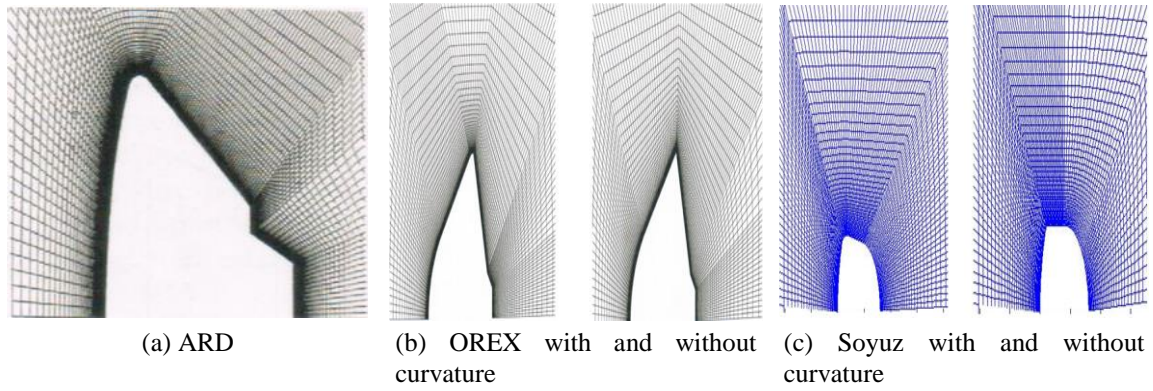


Fig. 3 Computational grid over the capsules

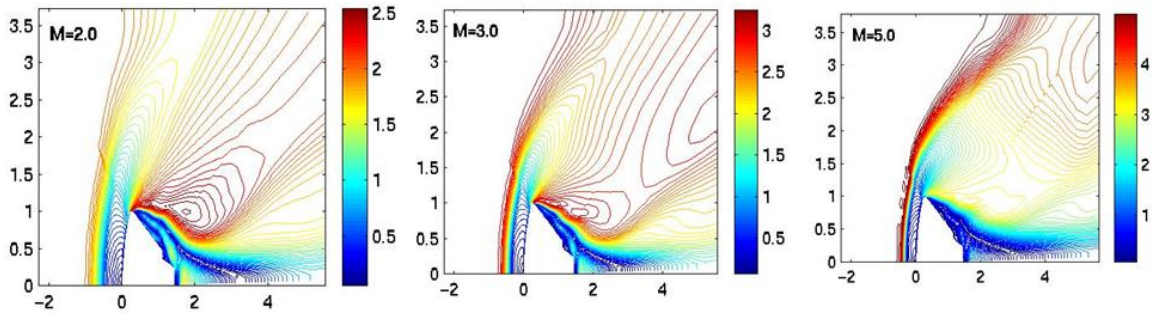


Fig. 4 Mach contour plots over the ARD

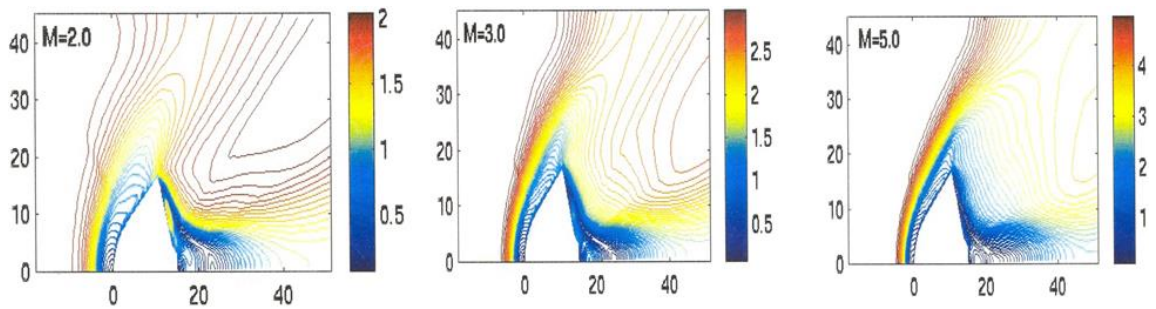


Fig. 5 Mach contour plots over the OREX capsule with curvature

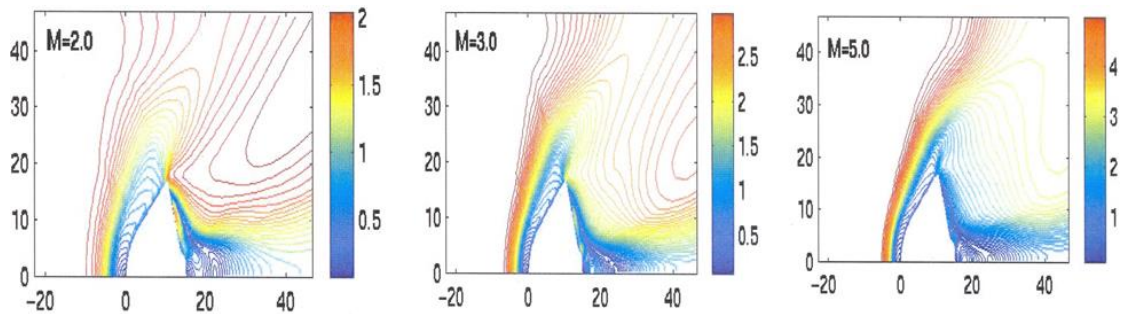


Fig. 6 Mach contour plots over OREX capsule without curvature

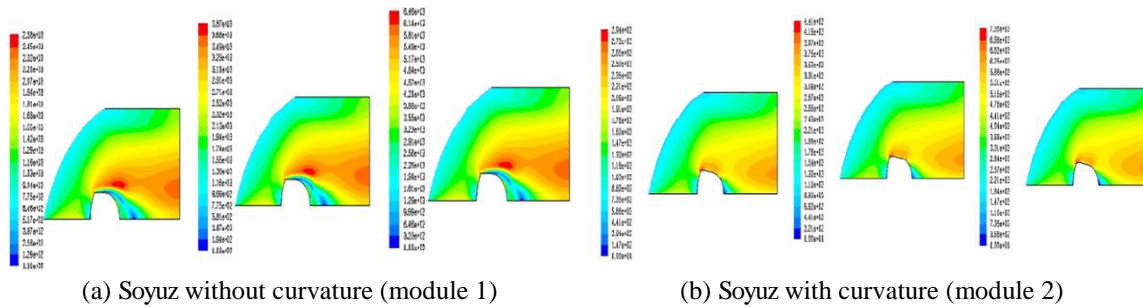


Fig. 7 Velocity contours over the Soyuz module 1 and the Soyuz module 2

value ρ at any grid point between two successive iterations $|\rho^{n+1} - \rho^n| \leq 10^{-5}$ where n is iterative index. This grid size has been arrived at on the basis of detailed grid independence test (Mehta 2006b).

5. Results and discussion

The numerical procedure mentioned in the previous section is applied to simulate the flow field over the ARD, the Soyuz and the OREX reentry capsules for freestream Mach numbers in the range of 2.0-5.0.

5.1 Flow characteristics

Figs. 4-6 show the computed Mach contours plot over the ARD and the OREX space reentry vehicles at various freestream conditions as mentioned in Table 1. It can be visualized from the Mach contour plots that all the significant flow field features such as bow shock wave, rapid expansion fans on the corner, flow recirculation region with converging free shear layer and formation of the vortex flow in the aft region of the space capsule. The wake flow field, immediately behind the capsule base, exhibits complex flow characteristics. The formation of the bow shock wave on the fore body of the capsule is observed, which depends on R_N and α_N and the value of M_∞ . The bow shock wave moves close to the fore body with increasing M_∞ and the stand-off distance between bow shock wave and the fore body decreases with the increasing M_∞ .

The bow shock wave follows the body contour and the fore body is entirely subsonic upto the corner tangency point of the ARD and the OREX where the sonic line is located. The Mach contour plots reveal many interesting flow features of the reentry capsule. The flow expands at the base corner and is followed by the recompression shock downstream of the base, which realigns the flow. The flow then develops in the trailing wake. The flow ground of the capsule is divided into regions inside and outside of the flow recirculating zone, and two regions are one vortex attached to the conical after-body frustum and a large recirculating vortex behind the reentry module.

The effect of shoulder radius R_C can be seen in Mach contour plots. A gradual flow turning can be visualized in the case of OREX with smooth shoulder edge as seen in Fig. 5 whereas a sharp flow turning is found in the sharp shoulder edge of the OREX as noticed in Fig. 6. The approaching supersonic boundary layer separates at the corner and the free shear layer is formed in

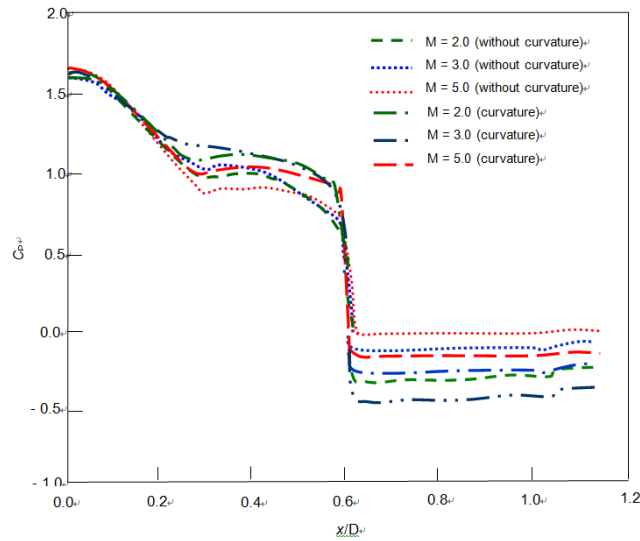


Fig. 8 Variation of pressure coefficient along the OREX capsule

the wake region. The wake flow features also depicts vortex attached to the corner with a large recirculating flow behind the vehicle adjacent to the axis of symmetry which depends on α_B and M_∞ . The separation point moves downward from the shoulder towards the base with the increase in M_∞ . The velocity flow field over the SOUYZ with and without shoulder radius is depicted in Fig. 7. The velocity plots show the effect of back shell inclination angle and shoulder radius. High velocity is observed with the shoulder radius and the back shell profile. The expansion waves concentrated at sharp shoulder of the OREX and the SOUYZ capsule as shown in Fig. 7(a) and Fig. 7(b). The leading and the tail waves are inclined to the direction of the flow angles corresponding to the upstream and downstream Mach numbers (Liepmann 2007). The expansion waves on the curved wall, the Mach wave forms a radial fan will have effect of the radius of the curvature, R_C . The effect of flow field in the aft region of the capsule will reveal in the variation of pressure over the surface that will be analyzed in the following section.

5.2 Surface pressure distribution

Figs. 8 and 9 display the pressure coefficient [$C_p = 2\{(p/p_\infty) - 1\}/(\gamma M_\infty^2)$] variation along the surface for the OREX, the ARD and the Soyuz capsules for $M_\infty = 2.0 - 5.0$. The $x/D = 0$ location is the stagnation point. The effects of geometrical parameters, such as radius of the spherical cap, half cone angle, with the sharp shoulder edge and with the smooth shoulder edge on the pressure coefficient are significant as can be seen from the variation of pressure coefficient along the capsules. A sudden drop in C_p is observed on the shoulder of the capsules followed by negative C_p variation in the base region. A low pressure is formed immediately downstream of the base which is characterized by a low speed circulating flow region which can be attributed to fill-up the region growing space between the shock wave and the body (Lighthill 1957). In the base region C_p is decreasing with increasing M_∞ . The effect of the corner radius on C_p can be observed in Figs. 8 and 9. The value of C_p is higher on the corner as compared with the sharp shoulder edge of the OREX module.

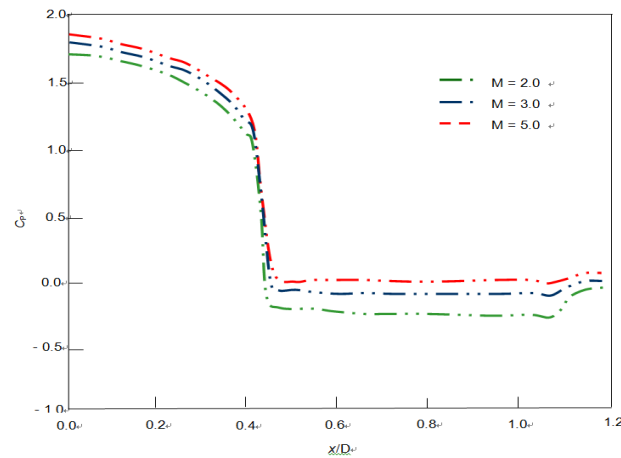


Fig. 9 Variation of pressure coefficient along the ARD capsule

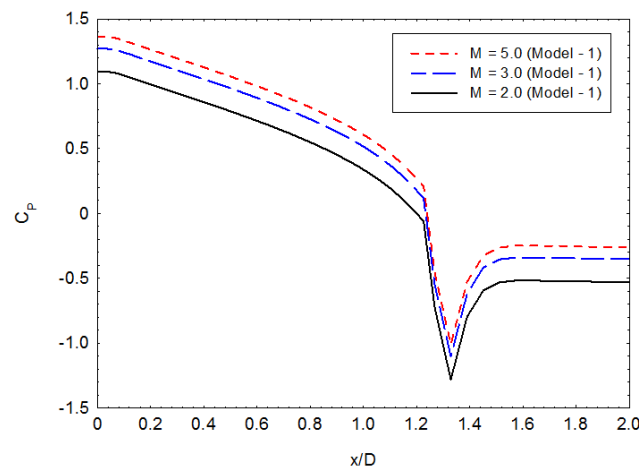


Fig. 10 Variation of pressure coefficient along the Soyuz capsule (without curvature)

The pressure coefficient on the spherical cap of the capsule decreases gradually for a given M_∞ . In Fig. 8, C_p falls on the sphere-cone junction and remains constant over the cone. In the case of the ARD and the OREX, the sonic point moves to the corner of the blunt bodies and affects the pressure distribution throughout the subsonic flow. In the case of the OREX with $\alpha_N=50^\circ$, the pressure coefficient shows over-expanded flow. The shoulder edge affects the corner expansion wave. The pressure coefficient variation along the surface and the integrated value of pressure coefficient will be useful quantities for optimization of the reentry capsule. The effect of R_C on the C_p variation over the OREX is depicted in Fig. 8. The variation of C_p is found in the conical and in the back-shell region.

Fig. 9 shows smooth variation of C_p distribution over the fore body of the ARD capsule. The effects of the fore body depend on the fore body shape as observed in the case of ARD and the OREX configuration of the capsules.

Figs. 10 and 11 display the pressure distribution over Soyuz module 1 (without shoulder radius) and Soyuz module 2 (with shoulder radius). It can be observed from the C_p variation that the

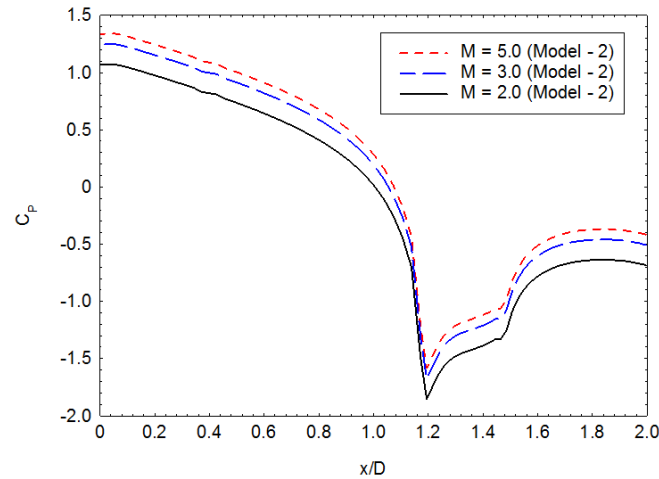


Fig. 11 Variation of pressure coefficient along the Soyuz capsule (with curvature)

geometrical parameters show significant effects on the surface pressure distributions. The variation of pressure coefficient on the spherical region decreases gradually for the Soyuz module 1 as compared to the Soyuz module 2. In the case of the module 2, the pressure coefficient shows over expanded flow on the shoulder due to presence of R_C . A drop of pressure coefficient is observed on the shoulder of the Soyuz module 1 and the Soyuz module 2 followed by the negative pressure coefficient variation in the base region. A low pressure is formed immediately downstream of the base, which is characterized by a low speed recirculating flow region. In the base region, the pressure coefficient is decreasing with increasing freestream Mach number. The effect of the corner radius on the pressure coefficient is higher. The C_p variation depends on the geometry of the capsules. The value of C_p in the back shell region of the Soyuz module 2 is low as compared with the Soyuz module 1, attributes to the influence of shoulder radius. The effect of the module geometrical parameters such as overall length L , fore-body diameter D , semi-cone angle of fore-body α_N and back-shell α_B and radius of shoulder curvature R_C on the pressure distribution and flow field features will be useful to compute ballistic coefficient.

5. Conclusions

The ratio of fore-body diameter to the overall length of the capsule, back shell half cone angle, with sharp shoulder edge with smooth shoulder edge on the flow-field have been numerically investigated for the ARD, the Soyuz and the OREX reentry capsules at supersonic Mach numbers range of 2.0-5.0. The flow fields over the reentry capsules are numerically simulated by solving compressible, laminar, and time-dependent the axisymmetric Navier-Stokes equations. A single-block structured is used in conjunction with finite volume flow solver. The essential flow field features are fairly well captured such as bow shock wave, expansion on the corner, recompression shock wave and recirculation flow in the base region. The configuration of the ARD, the Soyuz and the OREX reentry capsules resembles as a bell, a head light and a saucer shape, respectively and reveal different flow field features in the aft end of the capsules.

The flow field characteristics become complex due to the presence of shape the fore body,

corner at the shoulder and the back shell inclination angle of the reentry capsules. It is found that the shoulder of the capsule communicates flow from compression to expansion regions through the shoulder of the capsule, and the flow turns and expands rapidly, and boundary layer forming freestream layer that separates the inner recirculation flow zone behind the base from the outer flow field. The R_C and the α_B show significant effects on the wall pressure distribution over the capsule. The latter is recompressed and turned back to freestream direction. A low pressure is observed immediately downstream of the base which is characterized by a low-speed recirculating flow region. The pressure coefficients are important aerodynamic parameters for designing the capsule configuration.

References

- Ali, S.A., Husain, M. and Qureshi, M.N. (2012), "Effects of nose-bluntness ratio on aerodynamic performance for reentry vehicle", *J. Space Technol.*, **1**(1), 38-41.
- Bedin, A.P., Mishin, G.I. and Chistyakove, M.V. (1992), *Experimental Investigation of the Aerodynamic Characteristics and Geometric Parameters of Flows about Various Molecular Structures*, Nova Science Publishers, New York, U.S.A.
- Chen, B., Zhan, H. and Zhou, W. (2015), "Aerodynamic design of a reentry capsule for high speed manned reentry", *Acta Astronaut.*, **106**, 160-169.
- Chester, W. (1956), "Supersonic flow past a bluff body with a detached shock", *J. Flu. Mech.*, **1**(4), 353-365.
- Freeman, N.C. (1956), "On the theory of hypersonic flow past plane and axially symmetric bluff bodies", *J. Flu. Mech.*, **1**(4), 366-387.
- Ivanov, N.M. (1994), *Catalogue of Different Shapes for Un-Winged Reentry Vehicles*, Final Report, ESA Contract 10756/94/F/BM.
- Jameson, A., Schmidt, W. and Turkel, E. (1981), *Numerical Solution of Euler Equations by Finite Volume Methods Using Runge-Kutta Time Stepping Schemes*, AIAA 81-1259.
- Liepmann, H.W. and Roshko, A. (2007), *Elements of Gas Dynamics*, 1st South Asian Edition, Dover Publications Inc., New Delhi, India.
- Liever, P.A., Habchi, S.D., Burnell, S.I. and Lingard, J.S. (2003), "Computational fluid dynamics prediction of the beagle 2 aerodynamic data base", *J. Spacecr. Rockets*, **40**(5), 632-638.
- Lighthill, M.J. (1957), "Dynamics of a dissociating gas, part 1: Equilibrium flow", *J. Flu. Mech.*, **2**(1), 1-3.
- Mehta, R.C. (1998), "A quasi three dimensional automatic grid generation method", *Proceedings of the 25th National and International Conference on Fluid Dynamics and Fluid Power*, Delhi, India.
- Mehta, R.C. (2006a), "Numerical simulation of supersonic flow past reentry capsules", *Shock Waves*, **15**(1), 31-41.
- Mehta, R.C. (2006b), *Aerodynamic Drag Coefficient for Various Reentry Configurations at High Speed*, AIAA Paper 2006-3179.
- Mehta, R.C. (2008), "High speed flow field analysis for satellite launch vehicle and reentry capsule", *J. Magnetohyd. Plasma Space Res.*, **15**(1), 51-99.
- Minenkol, V.E., Agafonov, D.N. and Yakushev, A.G. (2015), "Project analysis of aerodynamics configuration of re-entry capsule-shaped body based on numerical methods for newtonian flow theory", *Aerosp. Sci. J. Bauman*, **4**, 1-14.
- Murphy, K.J., Bibb, K.L., Brauckmann, G.J., Rhode, M.N., Owens, B., Chan, D.T., Walker, E.L., Bell, J. H. and Wilson, T.M. (2011), "Orion crew module aerodynamic testing", *Proceedings of the 29th AIAA Applied Aerodynamics Conference*, Hawaii, U.S.A., June.
- Peyret, R. and Vivind, H. (1993), *Computational Methods for Fluid Flows*, Springer-Verlag, Berlin, Germany.
- Pezzelella, G. and Trifoni, E. (2015) "Aerodynamic analysis of high speed earth reentry capsule", *J. Aerodyn.*,

- 5(1), 34-68.
- Prasad, S. and Srinivas, G. (2012), "Flow simulation over re-entry bodies at supersonic and hypersonic speeds", *J. Eng. Res. Develop.*, **2**(4), 29-34.
- Ross, J.C. and Brauckmann, G.J. (2011), *Aerodynamic and Aeroacoustic Wind Tunnel Testing of the Orion Space Craft*, AIAA 2011-3160.
- Shang, J.S. (1984), "Numerical simulation of wing-fuselage aerodynamic interference", *AIAA J.*, **22**(10), 1345-1353.
- Solazzo, M.A., Sansone, A. and Gasbarri, P. (1994), "Aerodynamic characterization of the CARINA reentry module in the low supersonic regimes", *Proceedings of the 4th European Symposium on Aerothermodynamics for Space Applications*, Noordwijk, The Netherlands, November.
- Stremel, P.K., McMullen, M.S. and Garcia, J.A. (2011), *Computational Aerodynamic Simulations of the Orion Command Module*, AIAA 2011-3503.
- Viviani, A. and Pezzella, G. (2015), *Aerodynamic and Aerothermodynamic Analysis of Space Mission Vehicles*, Springer International Publishing A.G., Switzerland.
- Walpot, I. (2001), "Numerical analysis of the ARD capsule in S4 wind tunnel", *Proceedings of the 4th European Symposium on Aerothermodynamics for Space Applications*, Capua, Italy, October.
- Weiland, C. (2014), *Aerodynamic Data of Space Vehicles*, Springer-Verlag, Berlin Heidelberg, Germany.
- Wood, A.W., Gnoffo, P.A. and Rault, D.F.G. (1996), "Aerodynamic analysis of commercial experiment transport reentry capsule", *J. Spacecr. Rockets*, **33**(5), 643-646.
- Yamamoto, Y. and Yoshioka, M. (1995), *CFD and FEM Coupling Analysis of OREX Aero-Thermodynamic Flight Data*, AIAA 95-2087.
- Zhenmiz, Z., Yunliancy, D., Yi, L. and Tieliang, Z. (2011), "Shape optimization design method for the conceptual design of reentry vehicles", *Acta Astronaut. Sinica*, **32**(11), 1971-1979.

Nomenclature

C_D	Drag coefficient
C_P	Pressure coefficient
D	Fore-body diameter
d	Adapter diameter
E	Specific energy
F, G	Flux vectors
H	Source vector
k	Thermal conductivity
L	Overall length
M	Mach number
p	Static pressure
q	Heat flux
T	Temperature
t	Time
U	Conservative variables in vector form
u, v	Velocity components
R_N	Radius of sphere
R_C	Radius of shoulder
x, r	Coordinate directions
α_N	Semi-cone angle of fore-body
α_B	Semi-cone angle of back-shell
γ	Ratio of specific heats
μ	Molecular viscosity
ρ	Density
σ	Stress vector

Subscript

∞	Free-stream condition
----------	-----------------------